ISSN 1063-7826, Semiconductors, 2013, Vol. 47, No. 7, pp. 935–942. © Pleiades Publishing, Ltd., 2013.
Original Russian Text © V.A. Kulbachinskii, R.A. Lunin, N.A. Yuzeeva, I.S. Vasilievskii, G.B. Galiev, E.A. Klimov, 2013, published in Fizika i Tekhnika Poluprovodnikov, 2013, Vol. 47, No. 7, pp. 927–934.

SEMICONDUCTOR STRUCTURES, LOW-DIMENSIONAL SYSTEMS, AND QUANTUM PHENOMENA

Persistent Photoconductivity and Electron Mobility in $In_{0.52}Al_{0.48}As/In_{0.53}Ga_{0.47}As/In_{0.52}Al_{0.48}As/InP$ Quantum-Well Structures

V. A. Kulbachinskii[a]^, **R. A. Lunin**[a], **N. A. Yuzeeva**[a, c], **I. S. Vasilievskii**[b],
G. B. Galiev[c], **and E. A. Klimov**[c]

[a] *Department of Low-Temperature Physics and Superconductivity, Moscow State University, Moscow, 119991 Russia*
^e-mail: kulb@mig.phys.msu.ru
[b] *National Research Nuclear University MEPhI, Moscow, 115409 Russia*
[c] *Institute of Microwave Semiconductor Electronics, Russian Academy of Sciences, Moscow, 117105 Russia*

Submitted October 8, 2012; accepted for publication October 20, 2012

Abstract—The influence of the width of the quantum well L and doping on the band structure, scattering, and electron mobility in nanoheterostructures with an isomorphic $In_{0.52}Al_{0.48}As/In_{0.53}Ga_{0.47}As/In_{0.52}Al_{0.48}As$ quantum well grown on an InP substrate are investigated. The quantum and transport mobilities of electrons in the dimensionally quantized subbands are determined using Shubnikov–de Haas effect measurements. These mobilities are also calculated for the case of ionized-impurity scattering taking into account intersubband electron transitions. It is shown that ionized-impurity scattering is the dominant mechanism of electron scattering. At temperatures $T < 170$ K, persistent photoconductivity is observed, which is explained by the spatial separation of photoexcited charge carriers.

DOI: 10.1134/S1063782613070130

1. INTRODUCTION

In recent years, there has been intense development in both the scientific research and industrial implementation of microwave devices based on InAlAs/InGaAs nanoheterostructures grown on InP substrates. This is related to a number of advantages associated with the use of these structures in microwave equipment of which improved high-frequency characteristics and low noise are required [1, 2]. The possibility of increasing the InAs content in InGaAs layers to 70% and even higher enables not only the mobility and concentration of the electron gas in the channel to be enhanced, but the electron drift velocity to be significantly increased as well. This makes devices based on nanoheterostructures on InP substrates the most high-speed from those available today.

The current-gain cutoff frequency and noise factor of a high-electron-mobility transistor (HEMT) depend both on the geometrical parameters of the device (the gate width and gate–channel spacing) and the characteristics of the two-dimensional electron gas (the charge-carrier mobility and concentration). A high cutoff frequency and a low noise factor are attained mainly in HEMTs based on InAlAs/InGaAs heterostructures, in which electrons possess a smaller effective mass, the conduction-band discontinuity is larger, and the separation between the Γ and L valleys is also larger than in other heterostructures. InAlAs/InGaAs HEMTs can be fabricated both on GaAs substrates (pseudomorphic HEMTs (PHEMTs) and metamorphic HEMTs (MHEMTs)) and InP substrates (isomorphic (i.e., lattice-matched) and pseudomorphic). Using InP substrates, structures in which both the $In_yAl_{1-y}As$ and $In_xGa_{1-x}As$ layers are lattice-matched to the substrate can be grown. This is achieved for layer compositions with $y = 0.52$ and $x = 0.53$. The lack of strain in the layers relaxes restrictions on the layer thicknesses in these HEMT structures [3].

Measurements of the concentration and mobility μ of two-dimensional electrons and the device characteristics of lattice-matched InAlAs/InGaAs/InAlAs nanoheterostructures grown on InP substrates were carried out in [4]. A set of nanoheterostructures whose spacer thickness d_{sp} and quantum-well width L vary broadly (2 to 10 nm and 20 to 80 nm, respectively) was investigated. In [5], nanoheterostructures with an isomorphic $In_{0.52}Ga_{0.48}As$ channel ($L = 20$ nm, $d_{sp} = 2$ nm) grown on InP were used for improving the fabrication technology of microwave transistors.

The further development of nanoheterostructures grown on InP substrates has been related to the use of a pseudomorphic channel. Thus, PHEMT nanoheterostructures with an $In_{0.75}Ga_{0.25}As$ channel were studied in [6]. The channel, whose thickness varied from 20 to 35 nm, was enclosed by barrier and $In_{0.52}Al_{0.48}As$ buffer layers lattice-matched to the substrate. It was found that the electron mobility remains

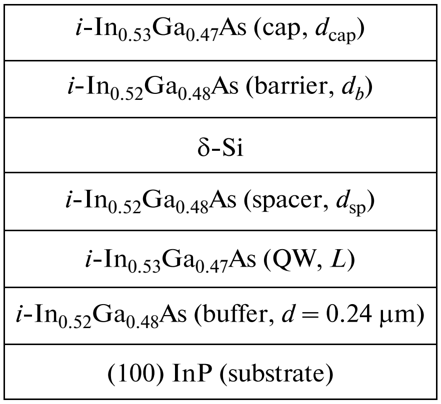

Fig. 1. Schematic layout of the structure.

independent of the well width and equal to $\mu \approx 11\,120$ cm^2/V s until $L = 20$ nm and decreases upon a further increase in L.

An increase in the electron mobility and, thus, in the frequency range of microwave transistors fabricated on InP substrates, can be attained using a pseudomorphic InGaAs channel with an In molar fraction x exceeding 0.52. Thus, structures with $x = 0.53$–0.80 were studied in [7] and structures with $x = 0.53$–0.74, in [8]. The channel width was 10–12 nm.

Increasing the frequency of a microwave transistor requires that the gate length be decreased and, in order to minimize the resulting short-channel effects, the quantum-well width be reduced and the well be located closer to the surface of the structure. In turn, a reduction in the well width leads to an increase in the energy gap between the dimensionally quantized subbands and, thus, to changes in the electron-scattering conditions. Thus, the problem of fabricating a transistor structure on the basis of an InP-compatible heterosystem involves such parameters as the quantum-well width, doping level, and electron concentration.

However, in our opinion, there has not been sufficient effort devoted to the comprehensive investigation of the electrical parameters of HEMT structures grown on InP substrates. In particular, there have been little studies in which Shubnikov–de Haas effect measurements were used to investigate in more detail the electron transport properties of $In_{0.52}Al_{0.48}As/In_yGa_{1-y}As/In_{0.52}Al_{0.48}As$ HEMT structures with an isomorphic $In_yGa_{1-y}As$ quantum well on an InP substrate.

Table 1. Technological parameters of the samples

Sample no.	L, nm	d_{sp}, nm	N(Si), 10^{12} cm^{-2}	d_b, nm
773	26	4.3	6.3	13.5
783	18.5	4.3	4.9	13.5
786	16	6.0	2.1	29
802	14.5	6.0	1.6	29

Note: Here, L is the width of the $In_{0.53}Ga_{0.47}As$ quantum well, d_{sp} is the spacer thickness, N(Si) is the concentration of the Si impurity in the δ-doped layer, and d_b is the barrier-layer thickness.

Here, we study in detail, in particular, with the use of Shubnikov–de Haas effect measurements at liquid-helium temperatures, isomorphic HEMT structures grown on InP substrates, and investigate changes in the band structure and the conditions of electron scattering taking place upon varying the width of the InGaAs quantum well and the doping level, and also under illumination.

2. SAMPLES AND EXPERIMENTAL TECHNIQUES

The samples under study were grown by molecular-beam epitaxy on (100)-oriented InP substrates. They represented $In_{0.52}Al_{0.48}As/In_{0.53}Ga_{0.47}As/In_{0.52}Al_{0.48}As/InP$ nanoheterostructures single-side δ doped with Si and having different widths L of the quantum well. The $In_{0.53}Ga_{0.47}As$ quantum-well layer, as well as all of the other $In_yAl_{1-y}As$ and $In_xGa_{1-x}As$ layers of the grown HEMT structures, was lattice-matched to InP. Figure 1 shows a schematic cross-sectional layout of the samples under study, and some of the sample parameters are listed in Table 1.

Different samples had different quantum-well widths L, spacer thicknesses d_{sp}, and barrier thicknesses d_b; the buffer thickness was the same in all samples and equal to 0.24 μm. The Si doping level in the δ layer also differed in different samples. Changes in the doping level were introduced because, upon a decrease in the well width, the energy of the upper dimensionally quantized subband increases and the electron wave function penetrates deeper into the InAlAs barrier, which leads to an increase in the scattering of electrons in the upper subband at ionized Si atoms in the barrier. For the same reason, the spacer thickness was somewhat increased in the samples with the narrowest quantum wells (samples 786 and 802).

The Hall effect was investigated at a temperature of 4.2 K in magnetic fields up to 6 T and at temperatures of 77 and 300 K in magnetic fields up to 0.6 T. The Shubnikov–de Haas effect was investigated at a temperature of 4.2 K in magnetic fields up to 6 T. The magnetic field was produced by a superconductive solenoid, as it was in the Hall-effect measurements at 4.2 K. In all cases, measurements were carried out for two opposite directions of the magnetic field in order to exclude the influence of sample resistance.

To examine the effect of illumination on the electrical parameters of the samples, a light-emitting diode with a wavelength of 668 nm was placed directly above the sample in the measurements of the temperature dependences of the resistivity and Shubnikov–

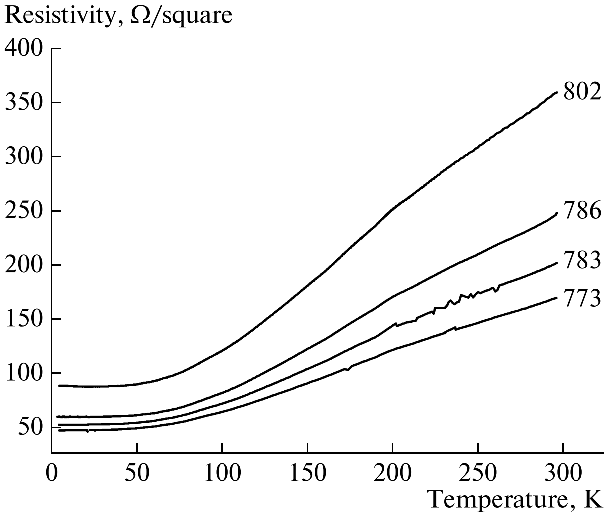

Fig. 2. Temperature dependences of the sheet resistivity.

de Haas effect. Photoconductivity relaxation was investigated at 4.2 K.

3. MEASUREMENT RESULTS AND DISCUSSION

3.1. Temperature Dependences of the Resistivity

The temperature dependences of the sheet resistivity for $T = 4.2–300$ K are shown in Fig. 2. For all samples, dependences typical of a degenerate electron gas were obtained.

At liquid-helium temperature, positive persistent photoconductivity was observed for all samples; it gradually disappeared at temperatures $T > 170$ K. Figure 3 shows the temperature dependences of the sheet resistivity for samples 783 and 802 in the dark and after illumination at 4.2 K, which was performed until the resistivity became saturated. After illumination, the sample was slowly warmed to room temperature.

3.2. Shubnikov–de Haas Effect

At liquid-helium temperature, the Shubnikov–de Haas effect was observed in all samples. For all of

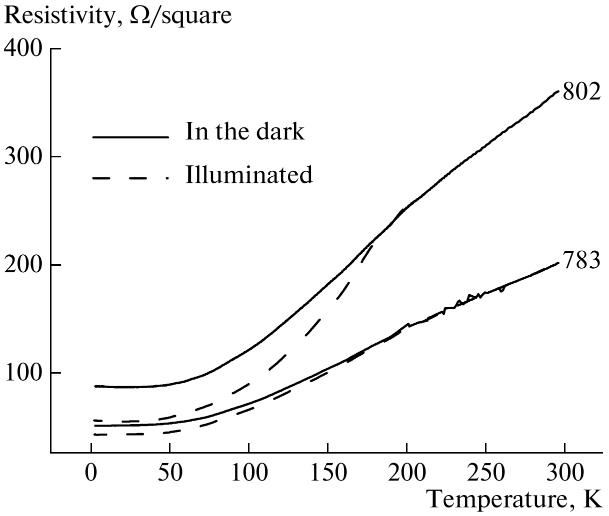

Fig. 3. Temperature dependences of the sheet resistivity for samples 783 and 802 in the dark (solid lines) and under illumination by light with a wavelength of 668 nm (dashed lines).

them apart from sample 802, the oscillations featured two frequencies, corresponding to the two occupied dimensionally quantized subbands. As an example, Fig. 4 shows magnetoresistance oscillations and their Fourier spectra for two samples. Table 2 lists the concentrations N_{Hall} and mobilities μ_{Hall} of electrons obtained from the Hall-effect measurements, as well as the electron concentrations N_{SdH} in the two subbands determined from the Shubnikov–de Haas effect (the values in parentheses pertain to the second subband). One can see that the Hall concentration agrees well with the sum of the concentrations in the two subbands determined from the Shubnikov–de Haas effect. This fact indicates that no parallel conduction along the δ layer takes place. The procedure by which the electron concentrations in the quantum-confinement subbands are determined was described in [9, 10]. It should be noted that, for all samples except sample 802, two dimensionally quantized subbands are occupied and two frequencies are manifested in the

Table 2. Concentrations N_{Hall} and mobilities μ_{Hall} obtained from the Hall-effect measurements and concentrations N_{SdH} obtained from the Shubnikov–de Haas effect measurements for the two subbands (except sample 802)

Sample no.	N_{SdH}, 10^{12} cm^{-2}	N_{Hall}, 10^{12} cm^{-2} (in the dark)			μ_{Hall}, cm^2 V^{-1} s^{-1} (in the dark)			μ_{Hall}, cm^2 V^{-1} s^{-1} (under illumination)
		300 K	77 K	4.2 K	300 K	77 K	4.2 K	4.2 K
773	2.5 (0.71)	3.13	3.12	3.25	11900	36100	40600	41000
783	2.0 (0.59)	2.51	2.50	2.60	11800	38900	45800	46900
786	1.67 (0.26)	2.10	2.07	1.95	12100	41900	53500	60000
802	1.55	1.57	1.55	1.56	10400	37000	45200	52400

Note: Values of N_{SdH} outside parentheses correspond to the first subband and the values in parentheses, to the second.

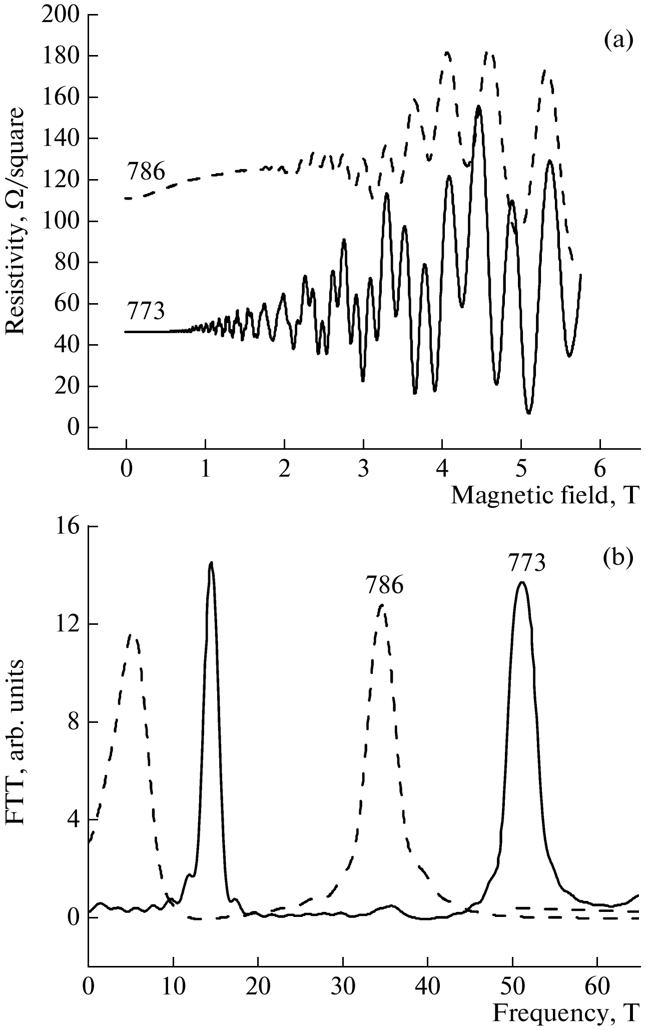

Fig. 4. (a) Magnetoresistance oscillations and (b) their Fourier transforms for samples 773 (solid line) and 786 (dashed lines). Two frequencies corresponding to the two occupied quantum-confinement subbands can be seen.

oscillations (see Fig. 4). The highest Hall mobility of electrons was observed in sample 786.

Illuminating the samples at liquid-helium temperature leads to an increase in the electron concentration in the quantum-confinement subbands. As an example, Fig. 5 shows the Shubnikov–de Haas oscillations in sample 786 in the dark and upon illumination. Note that, according to Table 2, apart from an increase in the concentration of electrons, illumination at $T = 4.2$ K leads to an increase in their Hall mobility.

Analysis of the temperature and magnetic-field dependences of the oscillation amplitude makes it possible to determine the quantum mobility μ_q and transport mobility μ_n of two-dimensional electrons in each of the subbands. Varying the values of μ_q and μ_n for each subband, one can fit the experimentally obtained magnetic-field dependences of the resistivity

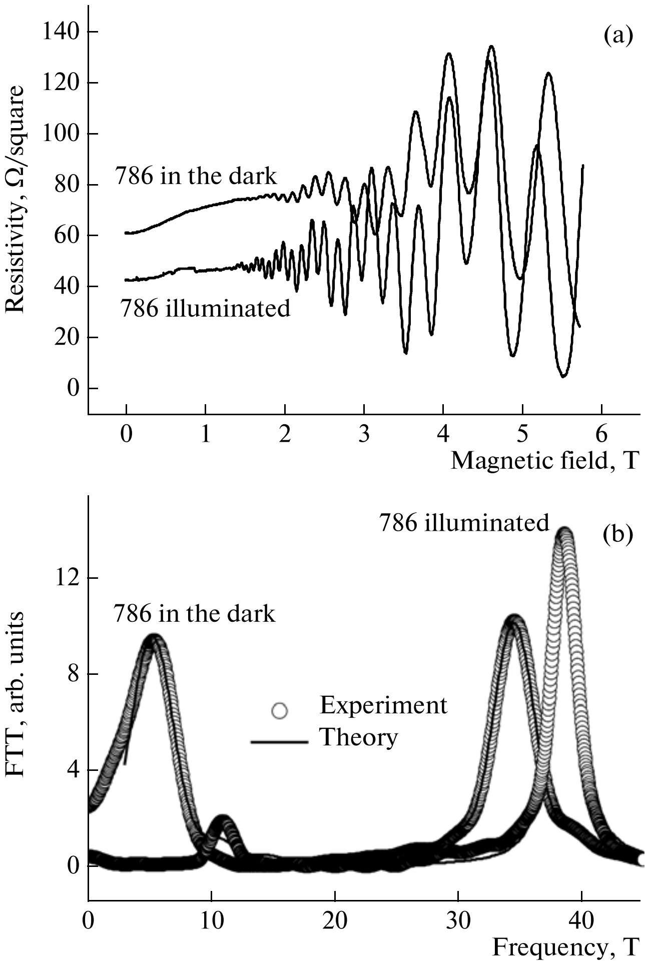

Fig. 5. (a) Shubnikov–de Haas oscillations and (b) their Fourier transform for sample 786 in the dark and under illumination.

and, thus, their Fourier transforms, according to the following formulas:

$$\sigma_{xx} = \frac{en_s\mu_n}{1+\mu_n^2B^2}\left[1+\frac{2\mu_n^2B^2}{1+\mu_n^2B^2}\frac{\Delta g(\varepsilon_F)}{g_0}\right], \qquad (1)$$

$$\sigma_{xy} = \frac{en_s\mu_n^2B}{1+\mu_n^2B^2}\left[1-\frac{3\mu_n^2B^2+1}{\mu_n^2B^2(1+\mu_n^2B^2)}\frac{\Delta g(\varepsilon_F)}{g_0}\right], \qquad (2)$$

$$\frac{\Delta g(\varepsilon_F)}{g_0} = 2\sum_{s=1}^{\infty}\exp\left(-\frac{\pi s}{\mu_q B}\right) \times \cos\left[\frac{2\pi s(E_F-E_i)}{\hbar\omega_c}-s\pi\right]\frac{(2\pi^2 s k_B T/\hbar\omega_c)}{\sinh(2\pi^2 s k_B T/\hbar\omega_c)}. \qquad (3)$$

Here, e is the elementary charge, $\mu_n = e\tau_n/m$ is the transport mobility of electrons for $B = 0$, $\mu_q = e\tau_q/m$ is the quantum mobility, τ_n and τ_q are the transport and quantum relaxation times, $\Delta g(\varepsilon_F)$ is the oscillating part

Table 3. Electron concentrations n_i in quantum-confinement subbands 1 and 2, quantum mobility μ_q, and transport mobility μ_n obtained from Shubnikov–de Haas effect measurements in the dark and under illumination at 4.2 K

Sample no.	Subband no.	n_i, 10^{12} cm^{-2} in the dark	n_i, 10^{12} cm^{-2} under illumination	μ_q, cm^2 V^{-1} s^{-1}		μ_n, cm^2 V^{-1} s^{-1}	
				in the dark	under illumination	in the dark	under illumination
773	2	0.70	0.74	8300	–	21000	–
	1	2.49	2.50	4300	–	23000	–
783	2	0.59	0.7	4400	5000	25000	32000
	1	2.00	2.20	2200	3500	28000	35000
786	2	0.26	0.53	3200	5200	30000	36000
	1	1.67	1.87	3200	5100	35000	44000
802	1	1.55	2.08	2100	2700	22000	40000

of the density of states at the Fermi level, g_0 is the density of states in the absence of magnetic field, and E_i is the energy of the bottom of the ith subband.

The results of the fit are shown in Fig. 5b by a solid line. The fitting procedure was based on the search optimization method described in [11], which minimizes the functions of many variables (up to 20) and features rapid convergence. Furthermore, the procedure yielding values for the mobilities converges stably, because μ_n and μ_q are responsible for different characteristics of the oscillations: μ_q mainly determines their decay as a function of the reciprocal magnetic field and μ_n, their amplitude. Table 3 summarizes the results on the quantum and transport mobilities of the charge carriers in each of the subbands in the dark and under illumination. Illumination leads to an increase in the electron concentration. The electron mobilities also increase since the screening of scattering centers is enhanced. The values thus obtained agree well with the experimental ones. The value of μ_n is somewhat lower than the experimental Hall mobility of electrons; this is caused by the limited accuracy of the method by which the mobilities are determined.

3.3. Calculation of the Band Diagram of the Structures

By solving self-consistently the Schrödinger and Poisson equations in a single-band effective-mass approximation for a temperature of 4.2 K, we determined the profile of the conduction-band bottom, the energy levels, and the electron wave functions [9, 10].

The wave functions $\psi_n(z)$ and energies E_n of the charge carriers were determined from the one-dimensional Schrödinger equation in the effective-mass approximation. This equation was solved using the transfer matrix technique [12]. The potential energy $U(z)$ is the sum of the discontinuity in the energy of the conduction-band bottom $U_c(z)$, the electrostatic potential (the Hartree potential) $U_H(z)$, and the exchange–correlation potential $U_{xc}(z)$. We have $U_c(z) = 490$ meV in $In_{0.52}Al_{0.48}As$ and $U_c(z) = 0$ in the $In_{0.53}Ga_{0.47}As$ quantum well [13–16]. The electron effective mass was taken to be $0.075m_0$ and $0.041m_0$ (where m_0 is the free-electron mass) in $In_{0.52}Al_{0.48}As$ and $In_{0.53}Ga_{0.47}As$, respectively [14–16]. The electrostatic potential was determined from the Poisson equation. The difference in the $In_{0.53}Ga_{0.47}As$ and $In_{0.52}Al_{0.48}As$ permittivities leads to the appearance of an image potential. However, this difference does not exceed 10%, and, thus, we did not take into account the contribution of this effect to the potential energy.

The calculation results are shown in Fig. 5 for samples 773 and 786 in the dark and sample 786 under illumination.

3.4. Photoconductivity Relaxation

As was noted above, all samples exhibited positive persistent photoconductivity at low temperatures (see Fig. 3). After switching the light off, the conductivity decreased relaxing to its original value. The kinetics of the photoconductivity relaxation in the samples under study was investigated at 4.2 K. As an example, Fig. 7 shows the time dependence of the photoconductivity in sample 786. This dependence can be well approximated by the formula $\sigma(0) - \sigma(t) = A\ln(1 + \frac{t}{\tau})$ [17–20]. Parameter τ amounts to tens of seconds and decreases with increasing temperature. This behavior corresponds to the spatial separation of photoexcited charge carriers. In the case under study, photogenerated electrons accumulate in the quantum well, and holes escape to the substrate and the surface. The latter fact leads to a reduction in the surface potential under illumination (see Fig. 6c). The fact that holes escape to the substrate causes partial flattening of the conduction band between the quantum well and the substrate.

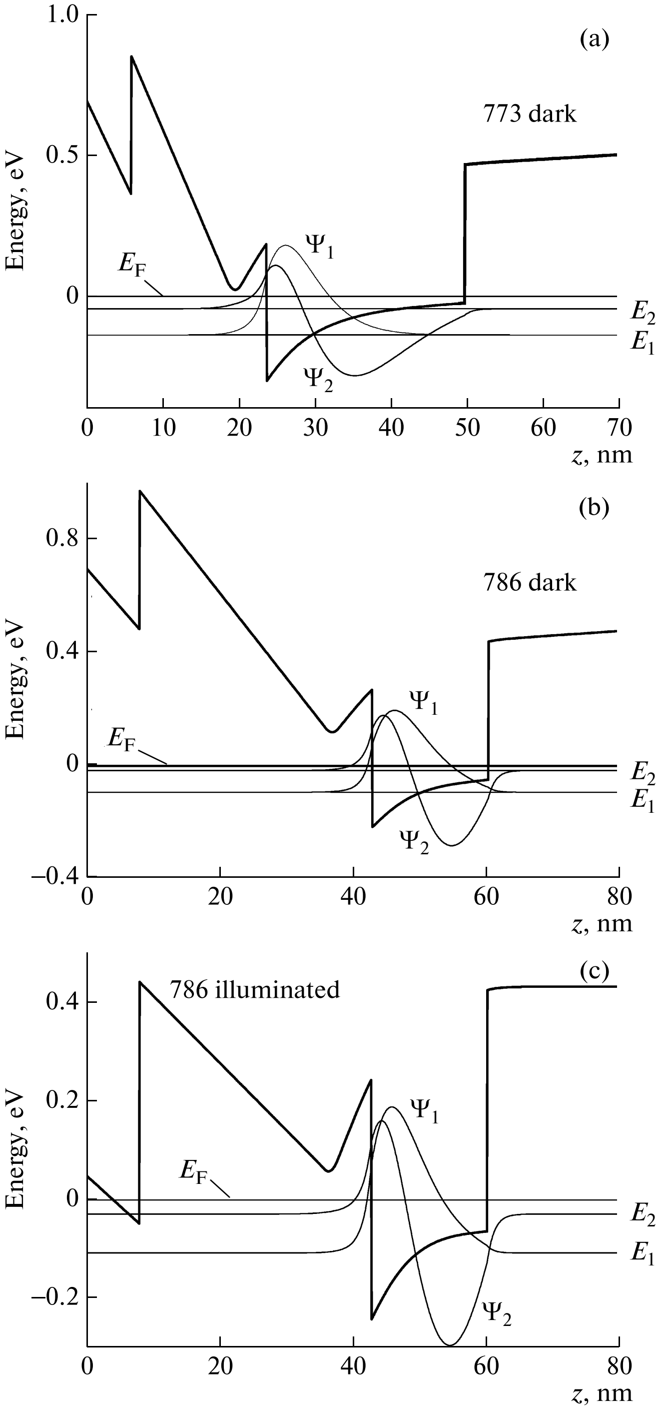

Fig. 6. Conduction-band profile, energy levels, and wave functions for the two quantum-confinement subbands in samples (a) 773 in the dark, (b) 786 in the dark, and (c) 786 under illumination. Energies are calculated from the Fermi level.

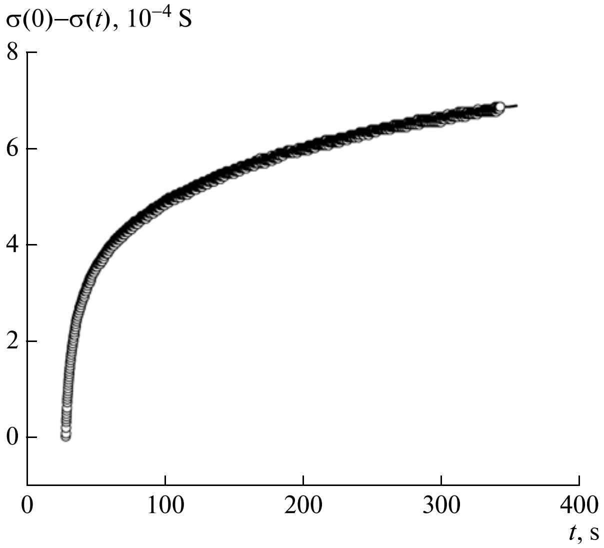

Fig. 7. Kinetics of photoconductivity relaxation in sample 786. Dots correspond to experimental points and the solid line shows the approximating curve.

3.5. Calculation of Electron Mobility Caused by Ionized-Impurity Scattering in the Case of Several Occupied Subbands

The transport mobility μ_n and quantum mobility μ_q can be determined by solving the kinetic equation and accounting for impurity scattering in the Born approximation. Scattering theory for the case where several subbands are occupied was set out in [21]. In the following, we describe the procedure for calculating the transport relaxation times τ_n (and, thus, μ_n) and the quantum relaxation times τ_q (and, thus, μ_q) of electrons in the subbands in the case of ionized-impurity scattering, taking into account intersubband transitions.

When several quantum-confinement subbands are occupied, τ_t is determined by the following set of linear equations:

$$P_n(E)\tau_n(E) - \sum_{n \neq n'} P_{nn'}(E)\tau_{n'}(E) = 1. \qquad (4)$$

Here, coefficients $P_n(E)$ are the probabilities of the corresponding intersubband transitions:

$$P_n(E) = \frac{m^*}{\pi\hbar^3}\int_0^{\pi} d\varphi(1-\cos\varphi)\left|\tilde{V}_{nn}(q)\right|^2 + \frac{m^*}{\pi\hbar^3}\sum_{n \neq n'}\theta(E-E_{n'})\int_0^{\pi} d\varphi\left|\tilde{V}_{nn'}(q')\right|^2, \qquad (5)$$

$$P_{nn'}(E) = \frac{m^*}{\pi\hbar^3}\theta(E-E_{n'})\left(\frac{E-E_{n'}}{E-E_n}\right)^{\frac{1}{2}} \times \int_0^{\pi} d\varphi\cos\varphi\left|\tilde{V}_{nn'}(q')\right|^2, \qquad (6)$$

Table 4. Quantum mobility μ_q and transport mobility μ_n calculated for samples 783 and 786 at $T = 4.2$ K in the dark and under illumination

Experimental conditions	Subband no.	N_{SdH}, 10^{12} cm^{-2}	μ_q, cm^2 V^{-1} s^{-1}	μ_n, cm^2 V^{-1} s^{-1}
		Experimental value		
		Sample 783		
In the dark	2	0.59	3300	62900
	1	2.0	1100	43300
Under illumination	2	0.74	5500	119000
	1	2.2	1600	75100
		Sample 786		
In the dark	2	0.26	3900	72000
	1	1.67	2100	86900
Under illumination	2	0.53	6700	183000
	1	1.87	2700	138000

where

$$q = 2k(1-\cos\varphi)^{\frac{1}{2}}, \quad q' = (k^2 - 2kk'\cos\varphi + k'^2)^{\frac{1}{2}},$$

$$k = \left[\frac{2m^*(E-E_n)}{\hbar^2}\right]^{\frac{1}{2}}, \quad k' = \left[\frac{2m^*(E-E_{n'})}{\hbar^2}\right]^{\frac{1}{2}},$$

and $\theta(x)$ is the Heaviside unit-step function.

The expression for the effective scattering potential takes into account the distribution of ionized impurities:

$$|\tilde{V}_{nn'}(q)|^2 = \int dz_i N(z_i)|\tilde{V}_{nn'}(q, z_i)|^2, \tag{7}$$

where $N(z_i)$ is the three-dimensional concentration of impurities at the point z_i.

Since ionized impurities are screened by free electrons from all occupied subbands, the matrix element of the unscreened Coulomb potential

$$V_{ll'}(q, z_i) = \frac{e^2}{2\varepsilon\varepsilon_0 q}\int \psi_l(z)\exp(-q|z-z_i|\psi_{l'}(z))dz$$

is related to the screening potential $\tilde{V}_{nn'}(q, z_i)$ via the dielectric function as follows:

$$\tilde{V}_{nn'}(q, z_i) = \sum_{ll'} \varepsilon^{-1}_{nn',\,ll'}(q)V_{ll'}(q, z_i);$$

here, ε_0 is the permittivity of free space, ε is the dielectric function of the medium, and $\psi_l(z)$ are the wave functions of the subbands calculated simultaneously with the energy-band diagram. In the random-phase approximation, the dielectric function can be written as follows:

$$\varepsilon_{ll',\,nn'}(q) = \delta_{ln}\delta_{l'n'} + \frac{e^2}{2\varepsilon\varepsilon_0 q}F_{ll',\,nn'}(q)\Pi_{nn'}(q). \tag{8}$$

Here, the form factor $F_{ll',\,nn'}$ is determined by the equation

$$F_{ll',\,nn'}(q) = \int dz \int dz' \psi_l(z)\psi_{l'}(z) \times \exp(-q|z-z'|)\psi_n(z')\psi_{n'}(z'). \tag{9}$$

and

$$\Pi_{nn'}(q, E_{\mathrm{F}}) = \frac{m^*}{\pi\hbar^2}\left[1 - \frac{C_+}{2}\left\{\left(\frac{E_{ij}}{E_q}+1\right)^2 - \left(\frac{2k_{\mathrm{F}_i}}{q}\right)^2\right\}^{\frac{1}{2}} + \frac{C_-}{2}\left\{\left(\frac{E_{ij}}{E_q}-1\right)^2 - \left(\frac{2k_{\mathrm{F}_i}}{q}\right)^2\right\}^{\frac{1}{2}}\right] \tag{10}$$

are polarization components for $T = 0$, where $E_{ij} = E_i - E_j$, $E_q = \dfrac{\hbar^2 q^2}{2m^*}$, $C_\pm = \mathrm{sgn}(E_{ij} \pm E_q)$, and k_{F_i} is the Fermi wave vector corresponding to the Fermi energy of the ith subband [22].

The transport mobility of electrons in the nth subband is given by the expression

$$\mu_n = \frac{e}{m^*}\langle\tau_n(E)\rangle,$$

$$\langle\tau_n(E)\rangle = \frac{\int \tau_n(E)E\dfrac{\partial f_0(E)}{\partial E}dE}{\int E\dfrac{\partial f_0(E)}{\partial E}dE}, \tag{11}$$

where f_0 is the Fermi–Dirac distribution function. The quantum mobility for the nth subband equals $\mu_q^{(n)} = \dfrac{e}{m^*}\tau_q^{(n)}$, where $\tau_q^{(n)}$ is the quantum lifetime of electrons at the Fermi level. This quantity is the inverse of the weighted sum of all scattering probabilities, i.e.,

$$\frac{1}{\tau_q^{(n)}} = \frac{m^*}{\pi\hbar^3}\sum_{n'}\int_0^{\pi} d\varphi\left|\tilde{V}_{nn'}(q')\right|^2. \qquad (12)$$

As an example, Table 4 presents the results of direct calculations of the quantum and transport mobilities for samples 783 and 786 assuming ionized-impurity scattering and taking into account intersubband transitions. Experimental values of the electron concentrations in the subbands were used. According to Table 4, both the electron concentrations and mobilities increase noticeably under illumination. Direct calculations agree well with the mobilities determined from the Shubnikov–de Haas effect measurements (see Table 3). The transport mobilities are considerably higher than the quantum mobilities. This fact is indicative of the dominant role of small-angle electron scattering, which is a feature typical of ionized-impurity scattering. Furthermore, the calculated values of the mobility are comparable to those determined experimentally (the difference does not exceed ~50%), and one may conclude that the contribution of scattering by remote ionized impurities is still quite significant in the structures under study. An additional contribution arises from alloy scattering in the InGaAs channel.

4. CONCLUSIONS

We have studied the mobilities of electrons in isomorphic $In_{0.53}Ga_{0.47}As$ quantum wells grown on InP substrates. The highest electron mobility is observed in quantum wells with a thickness of $d = 16$ nm. Data obtained from Shubnikov–de Haas effect measurements have been used to determine the quantum and transport mobilities of electrons in the quantum-confinement subbands. We have also calculated these mobilities theoretically for the case of ionized-impurity scattering taking into account intersubband transitions. The calculation results agree well with the experimental data. It has been shown that ionized-impurity scattering is the dominant scattering mechanism in the structures under study. At low temperatures, positive persistent photoconductivity has been observed. The kinetics of the photoconductivity relaxation demonstrate that it is caused by the spatial separation of charge carriers.

ACKNOWLEDGMENTS

This study was supported by the Ministry of Education and Science of the Russian Federation (state contract nos. 14.740.11.0869 and 16.513.11.3113). E.A. Klimov acknowledges the support of the V.G. Mokerov Foundation for Science and Education.

REFERENCES

1. Dong Xu, Heiner G. Heiß, Stefan A. Kraus, M. Sexl, G. Böhm, G. Trankle, G. Weimann, and G. Abstreiter, IEEE Trans. Electron Dev. **45**, 21 (1998).
2. T. Mimura, S. Hiyamizu, T. Fujii, and K. Nanbu, Jpn. J. Appl. Phys. **19**, L225 (1980).
3. P. R. Berger, P. K. Bhattacharya, and J. Singh, J. Appl. Phys. **61**, 2856 (1987).
4. A. S. Brown, U. K. Mishra, J. A. Henige, and M. J. Delaney, J. Vac. Sci. Technol. B **6**, 678 (1988).
5. K. Higuchi, H. Uchiyama, T. Shiota, M. Kudo, and T. Mishima, Semicond. Sci. Technol. B **17**, 475 (1997).
6. R. S. Sandhu, G. Bhasin, C. D. Moore, G. D. Uren, M. S. Goorsky, T. P. Chin, M. Wjtovich, T. R. Block, and D. C. Streit, J. Vac. Sci. Technol. B **17**, 1163 (1999).
7. Hanxuan Li, Ju Wu, Zhanguo Wang, Jiben Liang, Bo Xu, Qian Gong, Fengqi Liu, and Wei Zhou, J. Cryst. Growth **186**, 309 (1998).
8. W. Klein, G. Bohm, H. Heiss, S. Kraus, D. Xu, R. Semerad, G. Tränkle, and G. Weimann, J. Cryst. Growth **150**, 1252 (1995).
9. V. A. Kulbachinskii, R. A. Lunin, V. G. Kytin, A. S. Bugaev, and A. P. Senichkin, J. Exp. Theor. Phys. **83**, 841 (1996).
10. R. A. Lunin, V. G. Kytin, V. A. Kul'bachinskii, and G. A. Mironova, Vestn. Mosk. Univ., Ser. Fiz. Astron., No. 4, 31 (2007).
11. A. S. Rykov, *Search Optimization. Methods of Deformed Configurations* (Fizmatlit, Moscow, 1993) [in Russian].
12. B. Jonsson and S. T. Eng, IEEE J. Quant. Electron. **26**, 2025 (1990).
13. S. Bollaert, Y. Cordier, M. Zaknoune, T. Parenty, H. Happy, and A. Cappy, Ann. Telecommun. **56**, 15 (2001).
14. K. Satzke, G. Weiser, W. Stolz, and K. Ploog, Phys. Rev. B **43**, 2263 (1991).
15. R. Dittrich and W. Schroeder, Solid State Electron. **43**, 403 (1999).
16. J. T. Woo, J. H. Kim, T. W. Kim, J. D. Song, and Y. J. Park, Phys. Rev. B **72**, 205320 (2005).
17. H. Q. Queisser and D. E. Theodorou, Phys. Rev. B **33**, 4027 (1986).
18. V. A. Kulbachinskii, R. A. Lunin, V. G. Kytin, A. V. Golikov, A. V. Demin, V. A. Rogozin, B. N. Zvonkov, S. M. Nekorkin, and D. O. Filatov, J. Exp. Theor. Phys. **93**, 815 (2001).
19. V. A. Kulbachinskii, R. A. Lunin, V. A. Rogozin, V. G. Kytin, B. N. Zvonkov, S. M. Nekorkin, D. O. Filatov, and A. de Visser, Physica E **17**, 159 (2003).
20. V. A. Kulbachinskii, V. G. Kytin, V. A. Rogozin, B. N. Zvonkov, Z. M. Dashevskii, and V. A. Casian, Physica E **39**, 1 (2007).
21. E. D. Sigga and P. C. Kwok, Phys. Rev. B **2**, 1024 (1970).
22. K. Inoue and T. Matsuno, Phys. Rev. B **47**, 3771 (1993).

Translated by M. Skorikov